

Elemental abundances of 44 very metal-poor stars determined from Subaru/IRD near-infrared spectra

Wako AOKI^{1,2} Timothy C. BEERS³ Satoshi HONDA⁴ Tadafumi MATSUNO⁵ Vinicius M. PLACCO⁶
Jinmi YOON^{3,7} Masayuki KUZUHARA^{1,8} Hiroki HARAKAWA⁹ Teruyuki HIRANO^{1,2,8} Takayuki
KOTANI^{1,2,8} Takashi KUROKAWA^{8,10} Jun NISHIKAWA^{1,2,8} Masashi OMIYA^{1,8} Motohide TAMURA^{1,8,11}
Sébastien VIEVARD^{8,9}

¹National Astronomical Observatory, 2-21-1 Osawa, Mitaka, Tokyo 181-8588, Japan

²Astronomical Science Program, Graduate Institute for Advanced Studies, SOKENDAI, 2-21-1 Osawa, Mitaka, Tokyo 181-8588, Japan

³Department of Physics and Astronomy and JINA Center for the Evolution of the Elements, University of Notre Dame, Notre Dame, IN 46556, USA

⁴Nishi-Harima Astronomical Observatory, Center for Astronomy, University of Hyogo, 407-2 Nishigaichi, Sayo-cho, Sayo, Hyogo 679-5313, Japan

⁵Astronomisches Rechen-Institut, Zentrum für Astronomie der Universität Heidelberg, Mönchhofstraße 12–14, 69120 Heidelberg, Germany

⁶NSF NOIRLab, 950 N. Cherry Ave., Tucson, AZ 85719, USA

⁷Space Telescope Science Institute, 3700 San Martin Dr., Baltimore, MD 21218, USA

⁸Astrobiology Center, 2-21-1 Osawa, Mitaka, Tokyo 181-8588, Japan

⁹Subaru Telescope, 650 N. Aohoku Place, Hilo, HI 96720, USA

¹⁰Institute of Engineering, Tokyo University of Agriculture and Technology, 2-24-16, Nakacho, Koganei, Tokyo, 184-8588, Japan

¹¹Department of Astronomy, Graduate School of Science, The University of Tokyo, 7-3-1 Hongo, Bunkyo-ku, Tokyo 113-0033, Japan

*E-mail: aoki.wako@nao.ac.jp, timothy.c.beers.5@nd.edu, honda@nhao.jp, matsuno@astro.rug.nl, vinicius.placco@noirlab.edu, jyun@stsci.edu, m.kuzuhara@nao.ac.jp, harakawa@naoj.org, t.kotani@nao.ac.jp, tkuro@cc.tuat.ac.jp, jun.nishikawa@nao.ac.jp, omiya.masashi@nao.ac.jp, motohide.tamura@nao.ac.jp, vievard@naoj.org

ORCID: 0000-0002-8975-6829, 0000-0003-4573-6233, 0000-0001-6653-8741, 0000-0002-8077-4617, 0000-0003-4479-1265, 0000-0002-4168-239X, 0000-0002-4677-9182, 0000-0000-0000-0000, 0000-0003-3618-7535, 0000-0001-6181-3142, , 0000-0001-9326-8134, 0000-0002-5051-6027, 0000-0002-6510-0681, 0000-0003-4018-2569

Abstract

Abundances of five elements, Na, Mg, Al, Si, and Sr, are investigated for 44 very metal-poor stars ($-4.0 < [\text{Fe}/\text{H}] < -1.5$) in the Galactic halo system based on an Local Thermodynamic Equilibrium (LTE) analysis of high-resolution near-infrared spectra obtained with the Infrared Doppler instrument (IRD) on the Subaru Telescope. Mg and Si abundances are determined for all 44 stars. The Si abundances are determined from up to 29 lines, which provide reliable abundance ratios compared to previous results from a few optical lines. The Mg and Si of these stars are over-abundant, relative to iron, and are well-explained by chemical-evolution models. No significant scatter is found in the abundance ratios of both elements with respect to iron, except for a few outliers. The small scatter of the abundance ratios of these elements provides constraints on the variations of stellar and supernova's yields at very low metallicity. Al abundances are determined for 27 stars from near-infrared lines (e.g., 1312 nm), which are expected to be less affected by non-LTE (NLTE) effects than optical resonance lines. The average of the $[\text{Al}/\text{Fe}]$ ratios is close to the solar value, and no dependence on metallicity is found over $-3.0 < [\text{Fe}/\text{H}] < -2.0$. Na abundances are determined for 12 stars; they exhibit Solar abundance ratios and no dependence on metallicity. The Sr abundances determined from the Sr II triplet are significantly higher than those from the optical resonance lines obtained by previous studies for our sample. This discrepancy shows a clear dependence on temperature and surface gravity, supporting models that predict large NLTE effects on the near-infrared lines for metal-poor red giants.

Keywords: nuclear reactions, nucleosynthesis, abundances — stars: abundances — stars: Population II

1 Introduction

Elemental abundances of very metal-poor (VMP: $[\text{Fe}/\text{H}] < -2$)¹ and extremely metal-poor (EMP: $[\text{Fe}/\text{H}] < -3$) stars contain unique information on the details of nucleosynthesis pathways in the first generations of massive stars and supernova explosions

that constrain the ranges of their initial masses (McWilliam et al. 1995; Ryan et al. 1996; Nomoto et al. 2013; Ishigaki et al. 2018). The trend and scatter of elemental abundances of VMP stars trace the chemical evolution in the early stages of the Galaxy's formation.

Among a variety of elements, the abundance ratios of α -elements and iron ($[\alpha/\text{Fe}]$, e.g., $[\text{Mg}/\text{Fe}]$) have been used as an indicator of the contribution of type Ia supernovae compared to

¹ $[A/B] = \log(N_A/N_B) - \log(N_A/N_B)_\odot$, and $\log \epsilon_A = \log(N_A/N_H) + 12$ for elements A and B.

core-collapse supernovae. The $[\alpha/\text{Fe}]$ ratios of VMP stars could, however, reflect the yields of massive stars that are ejected by core-collapse supernovae, which depend on the stellar mass, explosion energy, and other factors related to the explosion mechanisms, while contributions of type Ia supernovae are not expected, due to their long timescales. However, observational results exhibit very small scatter in $[\text{Mg}/\text{Fe}]$ in VMP stars (e.g., Cayrel et al. 2004; Yong et al. 2013), except for a few outliers (e.g., Norris et al. 2001; Aoki et al. 2002b; Ivans et al. 2003). This suggests that the yields of early generations of massive stars are similar in α -elements and iron, and/or that the gas clouds from which VMP stars have formed were already well-mixed, homogenizing the $[\alpha/\text{Fe}]$ ratios. Si is another key element, because it is as abundant as Mg, and is related to both the static nucleosynthesis during stellar evolution and explosive nucleosynthesis in core-collapse supernovae. However, the abundance ratios of $[\text{Si}/\text{Fe}]$ in VMP stars are relatively uncertain, because spectral lines that are useful for abundance measurements for such stars are limited in the optical range (see below for more details). Further estimates of the scatter of the abundance ratios for other α elements are clearly desirable.

The abundance ratios of elements with odd atomic numbers, e.g., Na and Al, are sensitive to the surplus of neutrons during C-shell burning in massive stars, and depend both on the metallicity and adopted level of atmospheric overshooting (e.g., Kobayashi et al. 2006; Tominaga et al. 2007). The abundance ratios of these elements in VMP stars are uncertain compared to Mg, because there are fewer measurements for VMP stars, as the numbers of (optical) spectral lines that can be used for abundance measurements are relatively small. Large NLTE effects are expected for absorption-line formation for these spectral lines (e.g., Lind et al. 2022), which presents challenges for comparisons of measured abundance ratios with predictions by chemical-evolution models.

Sr is a key element to study the neutron-capture processes in the early stages of chemical evolution. Sr could be produced by many processes and sites, including the (main) r -process, the weak r -process (Wanajo & Ishimaru 2006, also known as the Lighter Elements Primary Process, LEPP; Travaglio et al. 2004), as well as the weak s -process in massive stars (e.g., Käppeler et al. 2011). Sr has two strong resonance lines in the blue spectral range (407.8 and 421.5 nm), which are detectable even for extremely metal-poor (EMP; $[\text{Fe}/\text{H}] < -3.0$) stars. However, these lines are too strong to determine accurate abundances in stars with relatively high metallicity ($[\text{Fe}/\text{H}] \gtrsim -2.0$) or with excesses of Sr. Sr abundances are less certain than abundances of another key neutron-capture element, Ba, which has weaker lines in the red spectral range in addition to the two strong resonance lines (455.4 and 493.4 nm).

We have previously reported on Si abundances determined from high-resolution spectra in the Y -, J - and H -bands obtained with the Subaru Telescope Infrared Doppler instrument (IRD; Tamura et al. 2012; Kotani et al. 2018) for six metal-poor stars (Aoki et al. 2022), demonstrating that reliable Si abundances can be determined using 10–30 spectral lines of Si I that are free from blending by other spectral features, opening a new window to investigate the abundance trends and scatter for Si in VMP and EMP stars. Aoki et al. (2022) also determined Sr abundances from the Sr II triplet lines for four stars among the six metal-poor stars. Whereas these Sr II lines in the near-infrared (NIR) range are free from blending and have strengths suitable for abundance measurements, the results exhibit some discrepancy from the Sr abundances determined from optical lines. This discrepancy may arise from NLTE effects for the NIR lines, as discussed by Andrievsky et al. (2011) and Bergemann et al. (2012). More systematic studies of Sr abun-

dances from NIR spectra covering a wider range of stellar parameters are also required to investigate the impact of NLTE effects on Sr abundance measurements. The Y -, J -, and H -bands include some other useful metallic lines that are detectable for VMP and EMP stars (e.g., Mg, Fe), although Aoki et al. (2022) focused on the above two elements.

Here we report abundance analyses of Si and Sr, as well as Na, Mg, Al, and Fe, for 44 metal-poor stars in the range of $[\text{Fe}/\text{H}]$ from -4.0 to -1.5 observed with the Subaru/IRD, including four of the six stars studied by Aoki et al. (2022). The sample selection and the IRD observations are reported in Section 2. Section 3 provides details of the abundance analyses and error estimates. The abundance results for Mg, Si, Na, and Al, and their trends with Fe, are discussed in Section 4. The Sr abundance results are compared with literature values obtained from optical Sr lines in this section, in which NLTE effects are discussed. The results are compared with predictions of Galactic chemical-evolution models in Section 5.

2 Sample and Observations

Bright metal-poor stars were selected from literature for the observations with Subaru/IRD. The list of the objects is provided in table 1. They are metal-poor stars that have been well-studied by previous works to determine elemental abundances from optical spectra. We focus on red giants, in which Si lines are detectable even in stars with very low metallicity (Aoki et al. 2022). The effective temperature (T_{eff}) and $[\text{Fe}/\text{H}]$ range from 4200 K to 5250 K and from -4.0 to -1.5 , respectively (see next section). The sample includes carbon-enhanced metal-poor (CEMP) stars (e.g., CS 30314-067, CS 29502-092). However, the excesses of carbon for these stars are not very significant, and no strong features of carbon-bearing molecules appear in the NIR spectra. Four of the six stars in Aoki et al. (2022) are included in the sample. The other objects are HD 25329, a cool main-sequence metal-poor star, and the CH star HD 201626, which could be affected by mass transfer from a companion AGB star.

The NIR spectra were obtained with the Subaru/IRD on March 15, 2022 and November 8, 2022 (UT). The spectra cover the Y -, J - and H -bands with spectral resolving power of $R \sim 70,000$, with about 2.4 pixel sampling of the resolution element. Examples of the spectra are shown in figure 1. The signal-to-noise (S/N) ratios per pixel are listed in table 1, as estimated from photon counts at 1050 nm and 1600 nm.

We extracted the one-dimensional spectra of our targets from the raw IRD data using a custom-made pipeline, as described in Aoki et al. (2022). The pipeline performs a series of data-reduction procedures (Kuzuhara et al. 2018; Kuzuhara et al., in preparation). These include subtraction of bias and correlated read noise, removal of scattered light, correction for flat-fielding, tracing of stellar spectra, and wavelength calibration using Th-Ar emission spectra whose wavelengths were from the atlas of Kerber et al. (2008). The pixel-to-wavelength relations were determined based on the Th-Ar lines and laser frequency comb spectra (Hirano et al. 2020).

Telluric absorption lines are identified by comparing the spectra of rapidly rotating early type stars, which exhibit only very broad and shallow absorption features, obtained in our observing program. Stellar spectral lines that are affected by telluric lines are excluded from the abundance analysis in the present work.

3 Abundance analysis

3.1 Spectral line data and equivalent-width measurements

Spectral line data of Si are given in Aoki et al. (2022), who adopted the data from VALD (Kupka et al. 1999) used by Fukue et al. (2021), based on Kelleher & Podobedova (2008). Ten lines in the *H*-band are supplemented from Afşar et al. (2016), who take transition probabilities also from Kelleher & Podobedova (2008) through NIST² for most of the lines. Fe lines in the *Y* and *J*-bands are also taken from the VALD data used by Kondo et al. (2019). Fe lines in the *H*-band are adopted from Ruffoni et al. (2013). The line data for Na, Mg, and Al are taken from Lind et al. (2022), who adopt the data from Biemont & Brault (1986) for Na, Pehlivan Rhodin et al. (2017) for Mg, and Mendoza et al. (1995) for Al. The line data for the Sr triplet are taken from Grevesse et al. (2015) as employed by Aoki et al. (2022). The line data, i.e., wavelengths, lower excitation potentials, and transition probabilities ($\log gf$ values), used in the analysis are listed in table 2.

Equivalent widths are measured by fitting Gaussian profiles to the line profiles for our giant stars. The results are listed in table 2 with the above line data. Following the procedure of Aoki et al. (2022), errors of the equivalent widths (σ_W) are estimated to be 0.2–0.9 pm, depending on the S/N ratios that range 50–300, by the formula of Norris et al. (2001) adopting $R = 70,000$, $n_{\text{pix}} = 10$. The errors are slightly larger than 1.0 pm for LAMOST J 0032+4107 and 2MASS J 0643+5934 that have S/N ratios lower than 50. The abundance errors due to these equivalent width errors are discussed in the next subsection.

3.2 Abundance determinations

Abundances of Na, Mg, Al, Si, Fe, and Sr are determined from the equivalent widths by a standard LTE analysis using model atmospheres from the ATLAS/NEWODF grid (Castelli & Kurucz 2003) and the radiative transfer code, which is based on the same assumptions as the model atmosphere program of Tsuji (1978), following the procedure of Aoki et al. (2022) for the analysis of Si and Sr abundances. The stellar parameters required for abundance analysis based on model atmospheres are taken from the literature, and listed in table 3. Effective temperatures (T_{eff}) and surface gravities ($\log g$) in this table are used with no modification in the analysis. This treatment is useful to compare the abundance results from our NIR spectra with those of previous studies from optical spectra, as for the Fe abundances described below. The $[\text{Fe}/\text{H}]$ values are re-determined for most of the objects using the equivalent widths of optical Fe lines reported in the literature (see below). The solar abundances reported by Asplund et al. (2009) are adopted to derive abundance ratios with respect to the solar values ($[\text{X}/\text{Fe}]$).

Examples of spectral lines used for abundance measurements are shown in Figure 2 with synthetic spectra for the abundance determined from the line and those for 0.15 dex higher and lower abundances. We note that the abundances are determined by the analysis of equivalent widths. This figure is shown to demonstrate the data quality and the sensitivity of the spectral features to abundance changes.

Fe abundances are also measured from NIR lines for most of the objects in our sample. The number of lines that can be used for the analysis is larger than 10 for only 9 objects in our sample, stars

that are relatively metal rich. The average number of NIR lines available for the other stars is about 3. By contrast, many Fe lines are available in the optical range, as studied by previous studies.

To obtain more reliable Fe abundances that are required to derive abundance ratios of elements with respect to Fe ($[\text{X}/\text{Fe}]$ values), we conducted a standard analysis using the equivalent widths of optical lines reported by previous studies for 40 stars for which they are available. The references are given in table 3. The table also lists the results ($[\text{Fe}/\text{H}]_{\text{opt}}$), the number of lines used in the analysis (N_{opt}), and the standard deviation of the Fe abundances derived from individual lines (σ_{opt}). We found good agreement between our results and previous studies ($[\text{Fe}/\text{H}]_{\text{ref}}$): The average and standard deviation of the differences between them for the 40 stars is 0.00 dex and 0.09 dex, respectively. We adopt the Fe abundances derived from the optical lines by our analysis for the 40 stars, and those from the literature for the remaining 7 stars, as the final results ($[\text{Fe}/\text{H}]_{\text{fin}}$).

We list the Fe abundances derived from the NIR lines for 41 stars in table 3 for reference. The results also agree well with those from optical lines in general. The average and standard deviations between the Fe abundances from the NIR lines and the above final results are -0.06 dex and 0.11 dex, respectively. Four objects exhibit discrepancies larger than 0.2 dex. The numbers of NIR lines used for the analysis for these four stars are smaller than six, which could result in relatively large uncertainties in Fe abundances derived from the IRD spectra.

Si abundances are determined for all 44 stars in our sample. The number of lines used in the analysis is from 14 to 29 for most of these stars. The exceptions are BD+44°493, LAMOST J2217+2104 and LAMOST J 0032+4107, for which the number of available lines is 12 or less (table 6), because of their extremely low metallicity or limited S/N ratio. Even for these stars, five or more clean lines in the NIR range are used in the analysis, which improves the reliability of the Si abundances in these stars.

Afşar et al. (2016) report elemental abundances from optical and NIR lines for two VMP stars, including HD 122563. The Si abundance ratios ($[\text{Si}/\text{Fe}]$) of HD 122563 derived from the five lines in the *H*-band used by their work and the present work are +0.46 and +0.50, respectively, demonstrating very good agreement.

Mg abundances are also determined from 2 to 8 lines for all 44 stars. The number of lines depends on metallicity and data quality, and is also significantly affected by the contamination from telluric lines, which are present in the same spectral regions as Mg. We note that the number of optical lines used to determine Mg abundances is usually less than 10. Hence, measurements from a few or several NIR lines could contribute to improving the reliability of Mg abundance determinations.

Lind et al. (2022) reported the Na, Mg, and Al abundances determined from optical and NIR lines for five stars, including HD 122563, by LTE and NLTE analyses. Five of the six Mg lines analyzed in the present work are also used to determine the abundance in their work. The averages of the Mg abundances ($\log \epsilon$ values) determined from the five lines for HD 122563 by the present work and the LTE analysis by Lind et al. (2022) are 5.27 and 5.25, respectively. The Mg abundance obtained from the same lines by their NLTE analysis is 5.28, indicating that NLTE effects are very small for this metal-poor red giant.

Afşar et al. (2016) also report the abundance results for Mg from optical and NIR lines. The Mg abundance ratio ($[\text{Mg}/\text{Fe}]$) of HD 122563 from the four lines used in their work and the present work are +0.46 and +0.45, respectively.

² National Institute of Standards and Technology: https://physics.nist.gov/PhysRefData/ASD/lines_form.html

Na abundances are derived from the Na I 1138 nm and 1140 nm lines. The lines are weak, and severely affected by telluric lines in many stars. As a result, the Na abundances are determined for only 12 stars. These lines are not well-studied previously, and no direct estimate of NLTE effects is reported. The estimates for other lines in the NIR range, which are summarized by Lind et al. (2022), indicate that the effect is on the order of 0.1 dex for unsaturated lines. As the Na I lines detected in our spectra are weak, the NLTE effects for our results are not expected to be significant.

Al abundances are determined for 27 stars. The number of lines found in the NIR range is at most six, and less than three in most cases. Hence, the abundance results are not as reliable as for Si and Mg. These lines are, however, still useful to determine Al abundances for VMP stars because only two optical Al I lines in the blue range are used in many cases of Al abundance studies for VMP stars, and large NLTE effects are anticipated for these lines (see next section).

The Al abundance ($\log \epsilon$ value) obtained for HD 122563 by Lind et al. (2022) from the 2 Al lines that are also measured by the present work is 3.75, which is 0.14 dex lower than our result (3.89). The equivalent widths of the two lines used in their work are smaller by about 40% than ours, which is the likely reason for this small difference in the abundance results. The reason for the discrepancy of equivalent widths between the two studies is not identified.

Sr abundances are determined for 40 stars in our sample. All three lines of the Sr II triplet are used in most cases. The remaining 4 stars include the two most metal-poor stars in our sample, BD+44°493 and LAMOST J2217+2104. Note our spectrum of LAMOST J0032+4107 has a relatively low S/N ratio. The other star is 2MASS J2016-0507, for which a very low Sr abundance ($[\text{Sr}/\text{Fe}] = -2.43$) is obtained by Hansen et al. (2018) from the optical lines. The NIR Sr II lines are not detectable in stars with such low Sr abundances.

We estimate the abundance changes for changes of the stellar parameters, $\Delta T_{\text{eff}} = 100$ K, $\Delta \log g = 0.3$ dex, $\Delta [\text{Fe}/\text{H}] = 0.3$ dex, and $\Delta v_{\text{turb}} = 0.5$ km s⁻¹ for HD 221170 and 2MASS J0954+5246, which represent relatively metal-rich ($[\text{Fe}/\text{H}] \geq -2.5$) and more metal-poor ($[\text{Fe}/\text{H}] < -2.5$) stars in our sample. These parameter changes are typical uncertainties estimated for VMP stars in previous studies (e.g. Honda et al. 2004). The sensitivity of derived abundances to the changes of stellar parameters is listed in table 4. The quadratic sum of the abundance changes for the four parameters ($\sigma_{\log \epsilon}$) is also provided in the table, along with the quadratic sum of the changes of abundance ratios ($[\text{X}/\text{Fe}]$) that is presented as $\sigma_{[\text{X}/\text{Fe}]}$. The $\sigma_{[\text{X}/\text{Fe}]}$ is adopted as the error for the abundance ratios of elements other than Fe. The error is dominated by the changes of micro-turbulent velocity and effective temperature (table 4).

The elemental abundances ($\log \epsilon$ and $[\text{X}/\text{Fe}]$), number of lines used in the analysis (N), standard deviation of abundances derived from individual lines (σ) and total errors including the errors due to uncertainties of atmospheric parameters ($\text{Error}_{\text{total}}$) are listed in tables 5, 6, 7, 8, and 9 for Mg, Si, Na, Al, and Sr, respectively. The σ values would include the errors due to uncertainties of equivalent widths, which is 0.1 dex or smaller for the data quality of the current sample (Section 3.1). The uncertainties of spectral line data are smaller than 0.1 dex (see the detailed estimates for the analysis of Si lines in Aoki et al. 2022). The random error of the abundance measurements is estimated by $\sigma N^{-1/2}$, which is included in the total error in the tables. The σ of Si I (σ_{Si}) is adopted in the estimates for element X for which the number of

lines available in the analysis (N_{X}) is small (i.e., the random error is $\sigma_{\text{Si}}/N_{\text{X}}^{1/2}$).

4 Results

4.1 Mg and Si

The top two panels of figure 3 show $[\text{Mg}/\text{Fe}]$ and $[\text{Si}/\text{Fe}]$, as a function of $[\text{Fe}/\text{H}]$, in the present work. For comparison, these panels also show the abundance ratios determined from optical lines by previous work for metal-poor stars, including substantial numbers of VMP and EMP stars (Cayrel et al. 2004; Yong et al. 2013; Jacobson et al. 2015). Mg abundance ratios obtained from NIR spectra in the present work agree quite well with those obtained by the previous work. The Mg-enhanced ($[\text{Mg}/\text{Fe}] = +1.33$) star at $[\text{Fe}/\text{H}] = -3.93$ is LAMOST 2217+2104 (Aoki et al. 2018), and the Mg-deficient ($[\text{Mg}/\text{Fe}] = -0.19$) one at $[\text{Fe}/\text{H}] = -2.03$ is the well known α -deficient star BD+80°245 (e.g., Ivans et al. 2003). Excluding these two stars, the averages (standard deviations) of $[\text{Mg}/\text{Fe}]$ in the ranges $-3.5 < [\text{Fe}/\text{H}] < -2.5$ and $-2.5 < [\text{Fe}/\text{H}] < -1.5$ are 0.46 (0.15) and 0.43 (0.10), respectively (see table 10). A shallow, but statistically significant, slope of $[\text{Mg}/\text{Fe}]$ is detected: $\delta[\text{Mg}/\text{Fe}]/\delta[\text{Fe}/\text{H}] = -0.10 \pm 0.05$.

The average of Si abundance ratios obtained from the NIR spectra agree well with that from optical spectra by the previous work. The scatter is, however, clearly smaller in the present results. We note that the Mg-enhanced star LAMOST J2217+2104 does not exhibit a remarkable excess of Si compared to other stars. Excluding BD+80°245, which also shows a significantly low Si abundance ratio, the averages (standard deviations) of $[\text{Si}/\text{Fe}]$ in the ranges $-3.5 < [\text{Fe}/\text{H}] < -2.5$ and $-2.5 < [\text{Fe}/\text{H}] < -1.5$ are 0.58 (0.14) and 0.51 (0.05), respectively (see table 10). The standard deviations are comparable with the measurement error for $[\text{Si}/\text{Fe}]$, which is typically 0.1 dex (table 6). Our study for a large number of NIR Si lines has revealed that the scatter of $[\text{Si}/\text{Fe}]$ is as small as that of $[\text{Mg}/\text{Fe}]$ in VMP stars. Table 10 also lists the averages and standard deviations of $[\text{Mg}/\text{Fe}]$ and $[\text{Si}/\text{Fe}]$ determined by the three studies based on optical spectra (Cayrel et al. 2004; Yong et al. 2013; Jacobson et al. 2015) shown in figure 3. The larger scatter of $[\text{Si}/\text{Fe}]$ than $[\text{Mg}/\text{Fe}]$ found by previous studies can be accounted for by the larger errors in measurements based on a few Si lines in the optical range. A shallow slope of $[\text{Si}/\text{Fe}]$ is also found: $\delta[\text{Si}/\text{Fe}]/\delta[\text{Fe}/\text{H}] = -0.08 \pm 0.04$. This result is compared with chemical-evolution models in §5.

The bottom panel of figure 3 shows $[\text{Mg}/\text{Si}]$, as a function of $[\text{Fe}/\text{H}]$. No significant scatter and trends are found in $[\text{Mg}/\text{Si}]$ over the metallicity range $-3.2 < [\text{Fe}/\text{H}] < -1.5$. Namely, Si exhibits almost an identical abundance trend as Mg in this metallicity range. We note that the $[\text{Mg}/\text{Si}]$ of BD+80°245 is indistinguishable from other metal-poor stars. On the other hand, the $[\text{Mg}/\text{Si}]$ of LAMOST J2217+2104 is higher than for other stars. The Si of this star is over-abundant ($[\text{Si}/\text{Fe}] = +0.75$), as found by Aoki et al. (2018), but it is not as significant as found for Mg ($[\text{Mg}/\text{Fe}] = +1.33$).

4.2 Na and Al

Figure 4 shows $[\text{Na}/\text{Fe}]$ and $[\text{Al}/\text{Fe}]$, as a function of $[\text{Fe}/\text{H}]$. The Na abundances are determined for only 10 stars in our study. The average of $[\text{Na}/\text{Fe}]$ is +0.17. This is lower than the results of previous studies for this metallicity range ($[\text{Fe}/\text{H}] > -3$), which mostly rely on the Na I D lines. Whereas the NLTE corrections for NIR

lines is 0.1 dex level (Lind et al. 2022), those for strong Na I D lines could be as large as -0.5 dex for very metal-poor stars, as reported by, e.g., Andrievsky et al. (2007) and Lind et al. (2011), as well as Lind et al. (2022), which could be the cause of the discrepancy between our results and previous ones.

Al abundances are determined for 27 stars from our NIR spectra. The averages and standard deviations of $[Al/Fe]$ are given in table 10. The average values are clearly higher than those obtained by previous studies for VMP stars from the optical Al I 394.4 nm and/or 396.1 nm lines by on the order of 0.5–1.0 dex. The Al abundance measurements from optical spectra have been reported for a limited number of stars in our sample. Figure 5 (top panel) compares the $[Al/Fe]$ obtained by the present work with the previous results from optical spectra for 12 stars (Honda et al. 2004, Roederer et al. 2014, Holmbeck et al. 2018, Johnson 2002, Fulbright 2000, Barklem et al. 2005, and Li et al. 2013).

This discrepancy in $[Al/Fe]$ could be due to NLTE effects, primarily for the optical lines. Nordlander & Lind (2017) have reported that the NLTE corrections for the Al abundances determined from the 394.4 nm and/or 396.1 nm lines are positive, and as large as 0.5 dex in VMP giant stars ($T_{\text{eff}} \leq 5000$ K, $\log g = 3$). On the other hand, small negative NLTE corrections are predicted for the NIR line at 1312.3 nm (Nordlander & Lind 2017). Larger effect is expected for the above two lines in the blue region for stars with lower metallicity. This might be found in the bottom panel of figure 5, which shows a correlation between the abundance differences between this work and literature as a function of metallicity. It should be noted, however, that the Al abundances of the two stars with highest metallicity in the figure are determined from weaker Al I lines in 700–900 nm (HD8724:Fulbright 2000; HD108577:Johnson 2002), for which the NLTE effects are expected to be much smaller than for the 394.4 nm and 396.1 nm lines. Further studies covering higher metallicity is required to examine the metallicity dependence of the NLTE effect. No clear correlation is found between the abundance differences and the stellar evolutionary status (T_{eff} and $\log g$) in figure 5.

The discrepancy between the Al abundances from NIR and optical lines is mostly resolved by the NLTE corrections. Since the NLTE effect for the NIR lines is predicted to be much smaller than those in the blue optical range, the results from the NIR lines should better trace the Al abundance trend than the values from the LTE analysis of optical lines. A comparison with chemical-evolution models is provided in § 5.

4.3 Sr

The Sr abundances are determined from the Sr II triplet in the J -band (1003.7 nm, 1032.7 nm, and 1091.5 nm) in the present work. Figure 6 shows $[Sr/Fe]$, as a function of $[Fe/H]$, for our sample and those determined by previous studies from the optical resonance lines. The $[Sr/Fe]$ values obtained by the present work are systematically higher than those from literature, as found in table 10. Figure 7 (top panel) compares $[Sr/Fe]$ values from this work and from the literature, indicating that the discrepancy is systematic, and is not clearly dependent on the $[Sr/Fe]$ values.

Aoki et al. (2022) have already reported the discrepancy of the Sr abundances from NIR and optical lines for HD 4306 and HD 221170. They demonstrated that the Sr abundance of the Sun derived by their analysis of the Sr II triplet reproduces the value obtained by Grevesse et al. (2015), concluding that the line data are not the reason for the discrepancy. On the other hand, large NLTE effects on the Sr II line formation have been reported for

cool red giants (e.g., Andrievsky et al. 2011; Bergemann et al. 2012). Hence, below we inspect the correlations between this abundance discrepancy and the stellar parameters in order to examine the NLTE models.

Figure 7 (lower three panels) shows the discrepancy of the $[Sr/Fe]$ abundance ratios between those from the NIR and optical lines, as a function of stellar parameters (T_{eff} , $\log g$, metallicity). There are clear dependencies of the discrepancy on T_{eff} and $\log g$: the discrepancy is larger in cooler and more evolved red giants. The discrepancy is as large as 1 dex, which is found for giants with the lowest temperature and gravity, for which a larger NLTE effect is predicted. An exception is 2MASS J0643+5934, which exhibits a discrepancy of 1.3 dex, although the temperature and gravity (4900 K and 2.5, respectively) are not very low in our sample. This star was studied by Bandyopadhyay et al. (2022) for the optical lines. Their Table 2 reports that the T_{eff} 's determined by the indicators other than that from the spectroscopic analysis of Fe I lines are lower than the adopted value (4900 K), e.g. 4600 K from the color $V - K$. Hence, the T_{eff} of this star might be lower than that adopted in their work. On the other hand, the $\log g$ values derived from all the methods, including that from Gaia parallax, are higher than 2.2 (their Table 3), suggesting that the $\log g$ value is robust. Hence, no clear reason for the large discrepancy of the Sr abundance found for 2MASS J0643+5934 is identified.

Andrievsky et al. (2011) present large negative NLTE corrections for $[Sr/Fe]$ abundance ratios from NIR infrared lines and smaller positive corrections for those from the optical resonance lines for cool red giants ($T_{\text{eff}} = 4500$ K and 5000 K). The difference of the corrections between the NIR and optical lines are as large as 0.5 dex. Similar NLTE corrections are demonstrated by Nordlander & Lind (2017) for metal-poor giants. The discrepancy found in the observational results from NIR lines (this work) and optical ones (the literature) are at least qualitatively explained by NLTE effects, supporting the NLTE calculations by the above work. For better understanding of the formation of optical and NIR Sr lines, further studies for individual Sr lines in stars with a variety of stellar parameters are desired.

5 Discussion and concluding remarks

We have determined Mg and Si abundances for 44 metal-poor stars from measurements of spectral lines identified in high-resolution NIR spectra. We found no statistically significant scatter for both $[Mg/Fe]$ and $[Si/Fe]$, excluding one or two outliers. Predictions of the yields from simulations of massive star evolution and core-collapse supernovae (e.g., Tominaga et al. 2007; Heger & Woosley 2010) indicate over-abundances of Mg and Si with respect to Fe in general, with dependence on the initial stellar masses.

The overall trend of the abundance ratios of Mg and Si are well-reproduced by the chemical-evolution models of Kobayashi et al. (2020). The averages of $[Mg/Fe]$ for stars in the ranges $-3.5 < [Fe/H] < -2.5$ and $-2.5 < [Fe/H] < -1.5$ of our sample are +0.46 and +0.43, respectively, whereas the $[Mg/Fe]$ values of their chemical-evolution models at $[Fe/H] = -3.0$ and -2.0 are both +0.45. We note that the α -poor star BD+80°245 is excluded from the statistics. We also note that $[Mg/Fe]$ exhibits a decreasing trend with increasing metallicity, while an almost constant over-abundance of Mg is predicted by chemical-evolution models. The slope reported in the previous section ($\delta[Mg/Fe]/\delta[Fe/H] = -0.10 \pm 0.05$) is estimated including the two most metal-poor stars with $[Fe/H] < -3.5$ (BD+44°493 and HE 1116-0634) that have relatively high $[Mg/Fe]$. If these two stars are excluded from

the statistics, the slope is not significant: $\delta[\text{Mg}/\text{Fe}]/\delta[\text{Fe}/\text{H}] = -0.05 \pm 0.05$.

The averages of $[\text{Si}/\text{Fe}]$ in the ranges $-3.5 < [\text{Fe}/\text{H}] < -2.5$ and $-2.5 < [\text{Fe}/\text{H}] < -1.5$ of our sample are $+0.57$ and $+0.50$, respectively, whereas the $[\text{Si}/\text{Fe}]$ values of the chemical-evolution models of Kobayashi et al. (2020) at $[\text{Fe}/\text{H}] = -3.0$ and -2.0 are $+0.58$ and $+0.51$, respectively, exhibiting almost perfect agreement. The decreasing trend of $[\text{Si}/\text{Fe}]$ with increasing metallicity ($\delta[\text{Si}/\text{Fe}]/\delta[\text{Fe}/\text{H}] = -0.08 \pm 0.04$) is also reproduced by the model. BD+80°245 is excluded from these statistics. We note for completeness that the trend does not change if the three most metal-poor stars are excluded.

A remarkable result of our study is the small scatter of $[\text{Si}/\text{Fe}]$. The small scatter of $[\text{Mg}/\text{Fe}]$ found by previous studies is also confirmed. Such small scatter in very metal-poor stars is not necessarily expected from the nucleosynthesis in early generations of massive stars and supernovae, because production environments of the three elements are different: Mg is produced in C burning during stellar evolution; Si is mostly produced in explosive O burning; Fe is produced by the complete Si burning. The ejected mass of Si and Fe depends on the fallback (e.g., Woosley & Weaver 1995; François et al. 2004). From the small scatter of $[\text{Mg}/\text{Fe}]$ found from their high-quality spectra, Cayrel et al. (2004) discuss that mixing of interstellar matter is efficient even at low metallicity (see also François et al. 2004). On the other hand, very large scatter of abundance ratios of neutron-capture elements, e.g., $[\text{Sr}/\text{Fe}]$ and $[\text{Ba}/\text{Fe}]$, are found in very metal-poor stars. This indicates relatively small variations of $[\text{Mg}/\text{Fe}]$ and $[\text{Si}/\text{Fe}]$ provided by individual supernovae (e.g., Scannapieco et al. 2022). Taking account of the dependence of those abundance ratios on progenitor mass, the mass ranges of progenitors that made dominant contributions to very metal-poor stars might be limited. As larger scatter is expected for those abundance ratios in most metal-poor stars (e.g., $[\text{Fe}/\text{H}] < -3.5$) because they would more clearly reflect the yields of individual supernovae, extension of measurements from NIR spectra to lower metallicity will be useful to examine this possibility.

There are two outliers: BD+80°245 exhibits very low $[\text{Mg}/\text{Fe}]$ and $[\text{Si}/\text{Fe}]$, and LAMOST J2217+2104 has a significantly high $[\text{Mg}/\text{Fe}]$. The abundance anomalies in these stars have been identified by previous studies based on optical spectra. Our study of NIR spectra confirms the anomaly of the Si abundance ratio of BD+80°245 with higher precision than the previous studies (e.g., Ivans et al. 2003). The low abundance ratios of both Mg and Si, as well as of Ca and Ti that were studied by previous work, suggest that Fe is enhanced in this object most likely by larger contributions of type Ia supernovae than other stars with similar metallicity.

The large excess of Mg, along with the moderate excess of Si in LAMOST J2217+2104, suggests that the mechanism that enhances Mg and Si in the progenitor of this object, which could be a supernova explosion of a first-generation massive star, is more or less different from that of core-collapse supernovae that have produced the typical abundance ratios found in metal-poor stars. This is a CEMP star with large excesses of N and O. Aoki et al. (2018) discuss that the elemental abundance pattern from C is best explained by the explosion of a massive star with $25 M_{\odot}$, which is not particularly different from typical mass of progenitors expected for bulk of metal-poor stars. Hence, there could be other unique features, e.g., rapid rotation or binarity, in the progenitor of this star. We note that our sample includes two CEMP stars with no excess of s-process elements, CS 29502-092 and CS 31014-

067 (Aoki et al. 2002a). Their abundance ratios of $[\text{Mg}/\text{Fe}]$ and $[\text{Si}/\text{Fe}]$, as well as $[\text{Sr}/\text{Fe}]$, are indistinguishable from those of other carbon-normal stars.

Our sample includes two r-II stars: CS 31082-001, and HE 1523-0901. Although the Mg and Si abundance ratios of HE 1523-0901 ($[\text{Mg}/\text{Fe}] = +0.25$ and $[\text{Si}/\text{Fe}] = +0.39$) are slightly lower than the averages, the departure is not statistically significant. The abundance ratios of CS 31082-001 agrees well with the averages. Our result supports the suggestions from previous studies based on optical spectra that there is no unique feature in the α/Fe abundance ratios in *r*-process enhanced stars (e.g., Roederer 2009). We note that the Sr abundances of these two stars are enhanced.

The $[\text{Al}/\text{Fe}]$ values in our work are flat within the errors ($\delta[\text{Al}/\text{Fe}]/\delta[\text{Fe}/\text{H}] = -0.02 \pm 0.09$). An increasing trend of $[\text{Al}/\text{Fe}]$ with increasing metallicity is expected in $[\text{Fe}/\text{H}] < -1$ because the production of odd-Z elements depends on the surplus of neutrons from ^{22}Ne (Kobayashi et al. 2020). Although such a trend is not found in our result, it is not excluded taking account of the errors due to small number of available lines and possible NLTE effects that are still uncertain. For the same reason, the size of the scatter is not well constrained by the present work. More comprehensive NLTE analyses of both optical and NIR Al lines will be useful to constrain the chemical evolution models.

This work demonstrates that high-resolution NIR spectra are useful to determine abundances of key elements in metal-poor stars. The Mg and Si abundances are well-determined by measurements of a larger number of spectral lines than available in the optical range. Measurements of NIR lines also contribute to examining the NLTE effects for Sr by providing additional transitions to the previous studies based on optical spectra. Our study focused on bright metal-poor stars that cover mostly the metallicity range with $[\text{Fe}/\text{H}] > -3.5$. The observation with IRD is, however, able to obtain sufficiently good spectra of stars with lower metallicity. For instance, Mg and Si abundances are well-determined for LAMOST J2217-2104 with $[\text{Fe}/\text{H}] = -3.9$ and $V = 13.4$. Further NIR observations of such most metal-poor stars will contribute to constraining the abundance trends and scatter produced by the first generations of stars.

Acknowledgments

This research is based on data collected at Subaru Telescope, which is operated by the National Astronomical Observatory of Japan. We are honored and grateful for the opportunity of observing the Universe from Maunakea, which has the cultural, historical and natural significance in Hawaii. We are grateful to Drs. Nozomu Tominaga and Miho N. Ishigaki for their useful comments on stellar yields and chemical evolution. This work was supported in part by the National Science Foundation under Grant No. OISE-1927130 (IReNA). W.A. is supported by JSPS KAKENHI grant No. 21H04499. T.C.B. acknowledges partial support from grant PHY 14-30152 (Physics Frontier Center/JINACEE), and OISE-1927130: The International Research Network for Nuclear Astrophysics (IReNA), awarded by the U.S. National Science Foundation. M.T. is supported by JSPS KAKENHI grant No.24H00242. The work of V.M.P. is supported by NOIRLab, which is managed by the Association of Universities for Research in Astronomy (AURA) under a cooperative agreement with the National Science Foundation.

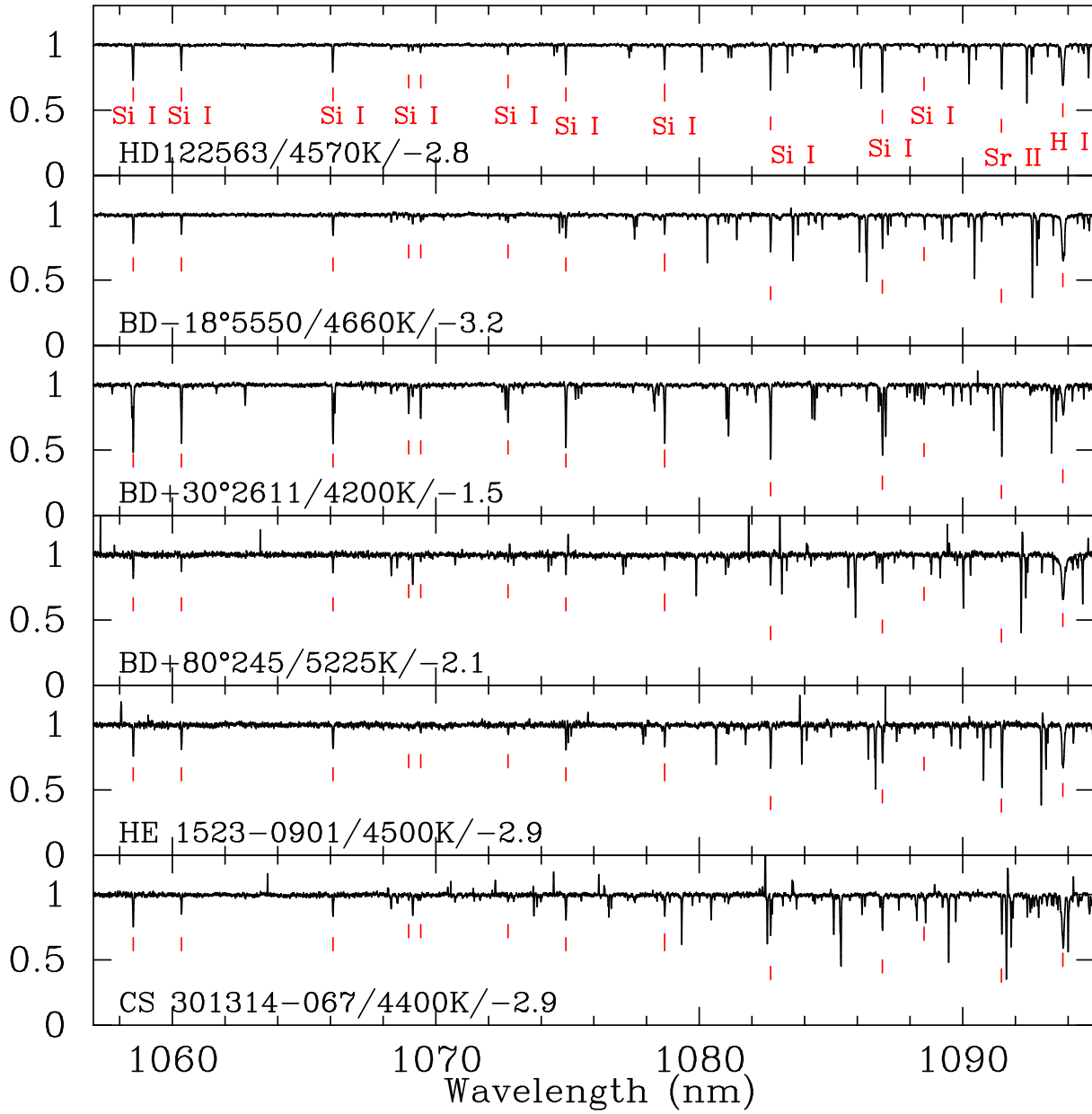


Fig. 1. Examples of near-infrared spectra obtained with Subaru/IRD. The star name, effective temperature, and metallicity are presented in each panel. The spectral lines of Si and Sr used for the abundance analysis, as well as a hydrogen line, are marked by red vertical bars. The CN absorption band at 1093–1095 nm is found for the carbon-enhanced star CS 30314-067. Alt text: Six line graphs showing the normalized spectra of six stars. The x axis shows the wavelengths from 1057 to 1095 nm. The y axis shows the normalized flux density.

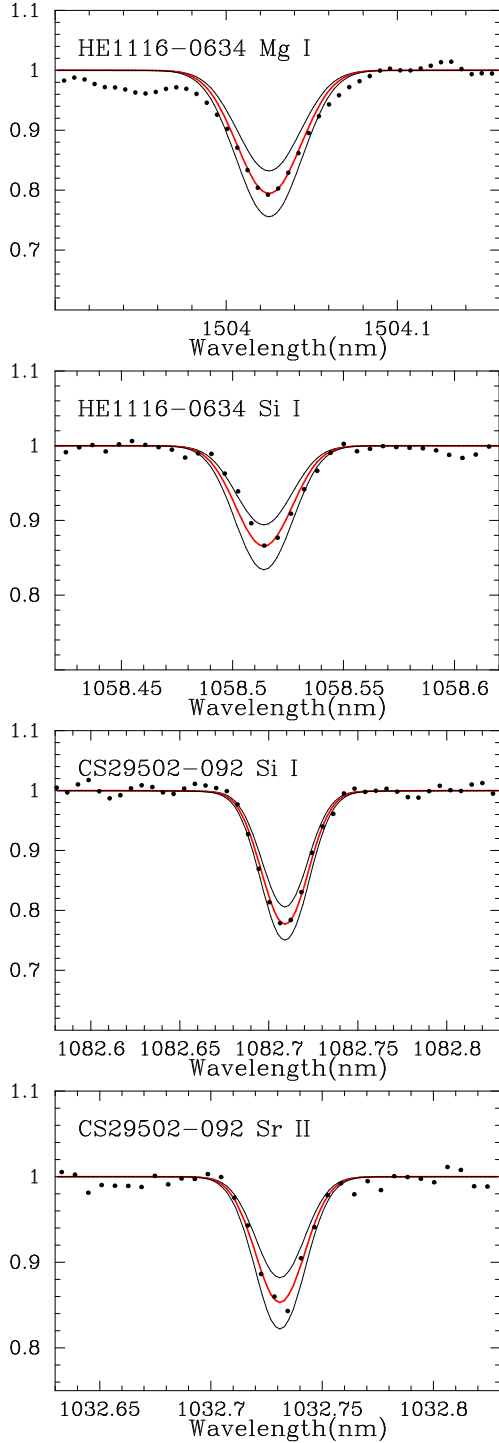


Fig. 2. Examples of spectral lines used for the abundance analysis (dots). The object name and the species are presented in the panels. The synthetic spectra for the abundance determined from the line and those changed by 0.15 dex are shown by solid lines. Alt text: Four graphs showing observed spectra and synthetic ones. The x axis shows wavelengths and the y axis shows normalized flux.

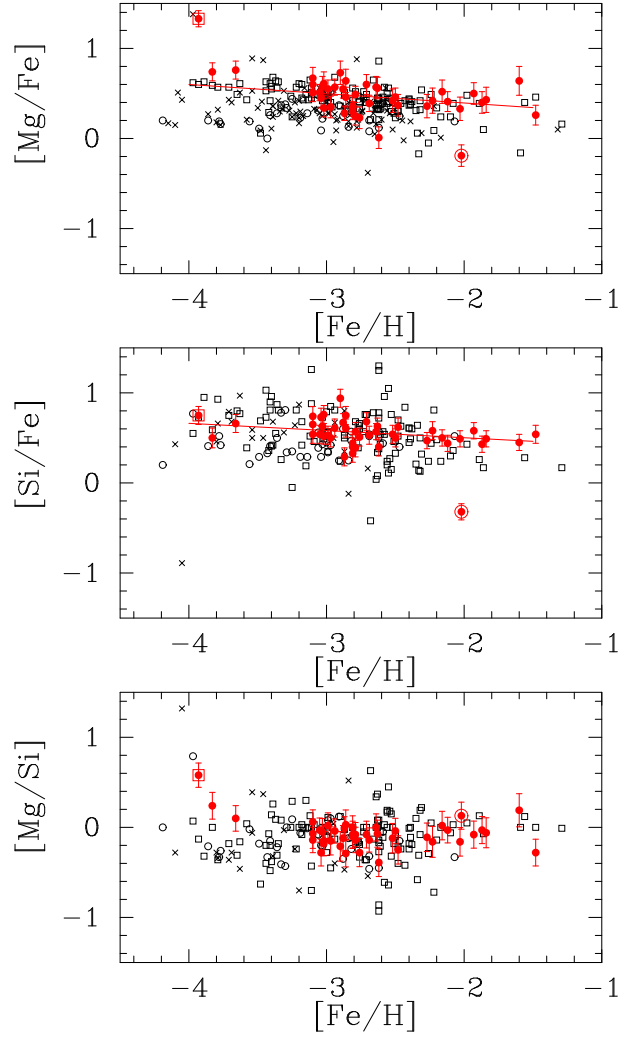


Fig. 3. $[Mg/Fe]$, $[Si/Fe]$, and $[Mg/Si]$, as a function of $[Fe/H]$. The results obtained by the present work are shown by filled circles. $[Mg/Fe]$ and $[Si/Fe]$ obtained by previous studies based on optical spectra are also shown in the corresponding panel by open circles: (Cayrel et al. 2004), crosses (Yong et al. 2013), and open squares (Jacobson et al. 2015). The α -deficient star BD+80°245 and the ultra metal-poor, carbon-enhanced star LAMOST J2217+2104 are shown by large open circles and open squares, respectively, over-plotted on the filled circles. The solid lines present the abundance trends obtained by least square fitting for the abundance ratios excluding the above two stars. Alt text: Three graphs showing abundance ratios $[Mg/Fe]$, $[Si/Fe]$ and $[Mg/Si]$. The x axis shows $[Fe/H]$ from -4.5 to -1.0 and the y axis shows the abundance ratios from -1.5 to $+1.5$.

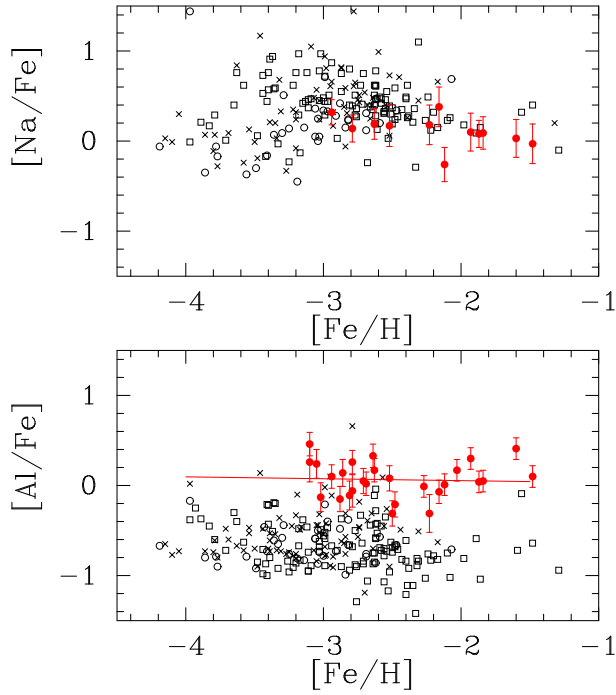


Fig. 4. The same as figure 3, but for $[\text{Na}/\text{Fe}]$ and $[\text{Al}/\text{Fe}]$. The abundance trend is not shown for $[\text{Na}/\text{Fe}]$ because the number of stars for which Na abundances are determined by the present work is too small. Alt text: Two graphs showing abundance ratios $[\text{Na}/\text{Fe}]$ and $[\text{Al}/\text{Fe}]$. The x axis shows $[\text{Fe}/\text{H}]$ from -4.5 to -1.0 and the y axis shows the abundance ratios from -1.5 to $+1.5$.

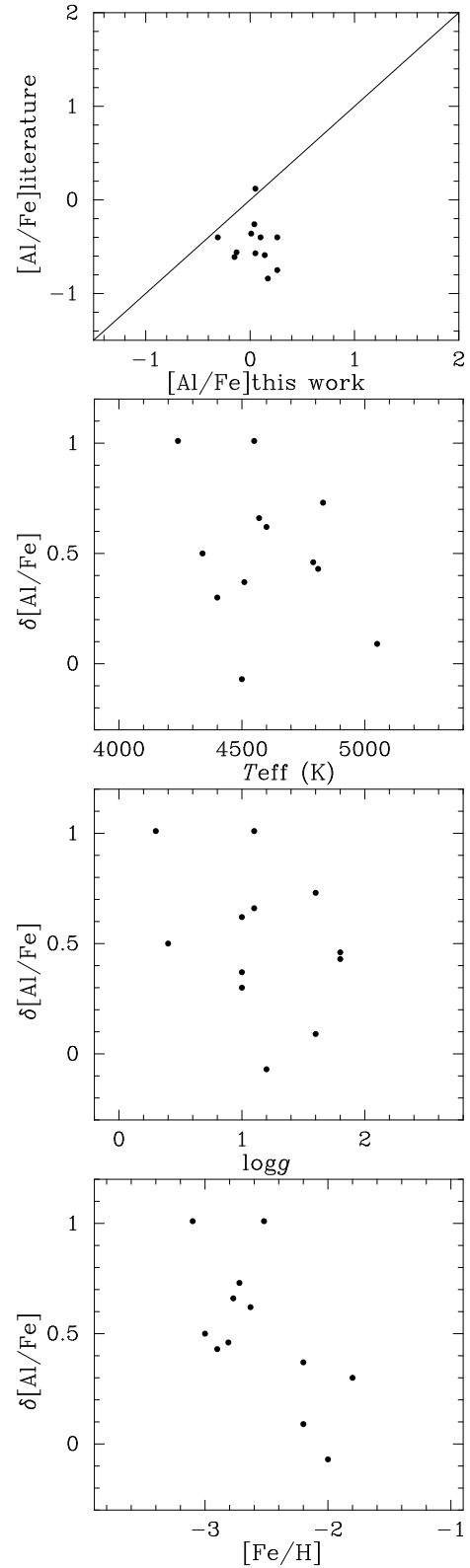


Fig. 5. (top panel) Comparison of $[\text{Al}/\text{Fe}]$ obtained by this work from the NIR spectra with those from optical lines in the literature. (2nd to 4th panels from the top) Differences of $[\text{Al}/\text{Fe}]$ between this work and literature ($\delta[\text{Al}/\text{Fe}] = [\text{Al}/\text{Fe}]_{\text{thiswork}} - [\text{Al}/\text{Fe}]_{\text{literature}}$), as functions of T_{eff} , $\log g$, and $[\text{Fe}/\text{H}]$. Alt text: A graph showing comparisons between abundance ratios $[\text{Al}/\text{Fe}]$. The x axis shows $[\text{Al}/\text{Fe}]$ determined by the present work from -1.5 to $+2.0$ and the y axis shows those from the literature from -1.5 to $+2.0$. Other three graphs showing differences of $[\text{Al}/\text{Fe}]$ values between this work and literature. The x axis shows stellar parameters and abundance ratios. The y axis shows the abundance differences.

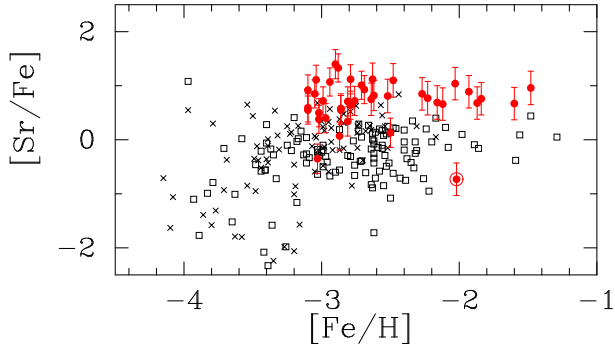


Fig. 6. The same as figure 3, but for $[\text{Sr}/\text{Fe}]$. The abundance trend is not shown because the Sr abundances determined from NIR lines are severely affected by NLTE effects (see text). Alt text: A graph showing abundance ratios $[\text{Sr}/\text{Fe}]$. The x axis shows $[\text{Fe}/\text{H}]$ from -4.5 to -1.0 and the y axis shows the abundance ratios from -2.5 to $+2.5$.

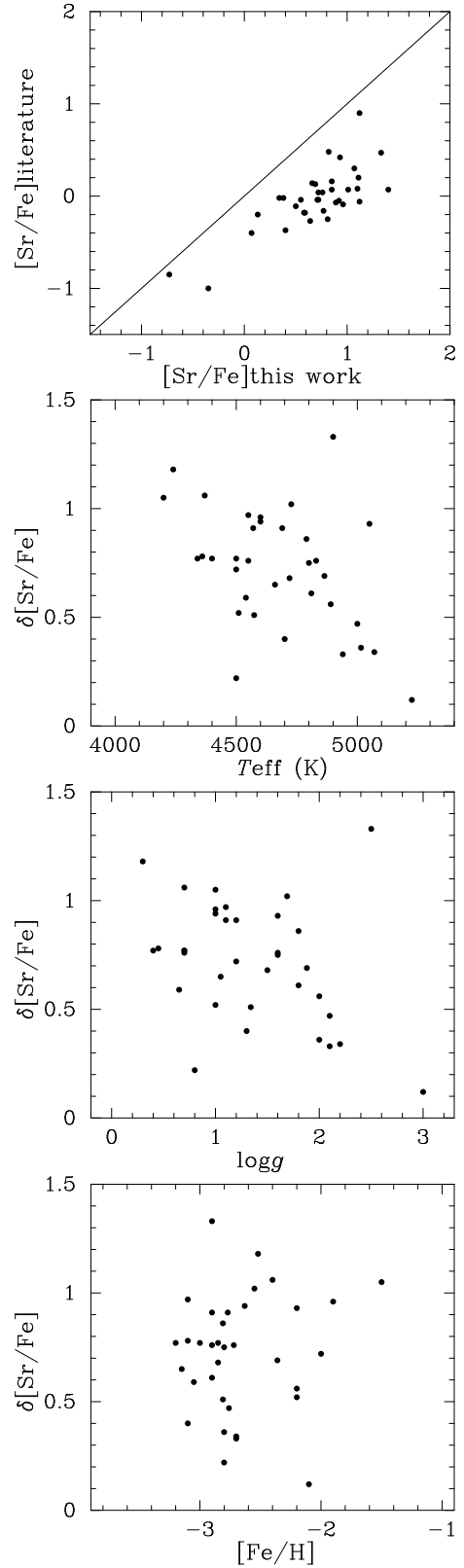


Fig. 7. The same as figure 7, but for Sr.

Table 1. Objects and Observations

Star	Gaia ID	Obs. Date (UT)	Exp. Time (sec)	S/N (1050nm)	S/N (1600nm)
HD 4306	2473977823368495360	Jul. 25, 2020	180	57	78
HD 6268	5033960575837265920	Nov. 8, 2022	120	75	115
HD 8724	2593188145361730432	Nov. 8, 2022	120	78	116
HD 13979	5118012879660872832	Nov. 8, 2022	300	91	132
HD 85773	5660878702718068864	Mar. 15, 2022	300	120	182
HD 88609	851658896305185024	Mar. 15, 2022	180	110	165
HD 107752	3907404496774653312	Mar. 15, 2022	630	109	154
HD 108577	3907872613852996864	Mar. 15, 2022	420	93	130
HD 110184	3710786979933623424	Mar. 15, 2022	120	98	155
HD 115444	1474455748663044736	Mar. 15, 2022	300	116	175
HD 118055	3603949359207346048	Mar. 15, 2022	300	164	257
HD 122563	3723554268436602240	Mar. 15, 2022	60	202	297
HD 187111	4189688954569244032	Nov. 8, 2022	60	115	186
HD 204543	2672702897842335872	Nov. 8, 2022	180	144	214
HD 221170	2869759781250083200	Jul. 25, 2020	120	134	230
HD 237846	1049376272667191552	Mar. 15, 2022	600	103	141
BD+03°2782	3712682602403001728	Mar. 15, 2022	600	97	165
BD+30°2611	1275876252107941888	Mar. 15, 2022	180	110	173
BD+44°493	341511064663637376	Jul. 25, 2020	900	187	253
BD+80°245	1139085117140997120	Mar. 15, 2022	900	69	89
BD−02°5957	2643630302870307328	Nov. 8, 2022	900	58	86
BD−07°2674	5755996908175855232	Mar. 15, 2022	600	100	149
BD−14°5890	6888560851915102464	Nov. 8, 2022	600	88	124
BD−15°5781	6887351938881045504	Nov. 8, 2022	900	48	67
BD−18°271	2450584991932903168	Nov. 8, 2022	300	92	148
BD−18°5550	6867802519062194560	Nov. 8, 2022	540	116	188
BD−20°6008	6857966322398347008	Nov. 8, 2022	360	79	115
CS 29502−092	2629500925618285952	Nov. 8, 2022	1800	61	91
CS 30314−067	6779790049231492096	Nov. 8, 2022	1800	87	130
CS 31082−001	2451773937663757696	Nov. 8, 2022	2400	58	120
HE 1116−0634	3783989199935482624	Mar. 15, 2022	1800	91	137
HE 1320−1339	3608447014600045824	Mar. 15, 2022	900	91	132
HE 1523−0901	6317828550897175936	Mar. 15, 2022	480	54	101
LAMOST J003251.47+410749.0	381063654713703040	Nov. 8, 2022	900	22	35
LAMOST J004012.52+272924.7	2809551447929127040	Nov. 8, 2022	1350	84	121
LAMOST J074847.30+461308.4 (TYC 3407-1352-1)	927340854329737216	Mar. 15, 2022	900	60	89
LAMOST J210958.01+172544.0	1788003032879354752	Nov. 8, 2022	600	69	103
LAMOST J211401.52−061610.3	6910940758263238912	Nov. 8, 2022	900	81	117
LAMOST J221750.59+210437.2	1778804140643594240	Jul. 25, 2020	5400	73	110
LAMOST J234759.59+285130.7	2866981452805072640	Nov. 8, 2022	1350	71	94
2MASS J06430186+5934309 (TYC 3778-529-1)	1001955470034395776	Mar. 15, 2022	900	22	30
2MASS J09544277+5246414 (TYC 3814-1598-1)	828438619475671936	Mar. 15, 2022	420	98	150
2MASS J20165357−0503592 (UCAC4 425-121652)	4219051451239614080	Nov. 8, 2022	1800	52	85
2MASS J21454816+1249124 (UCAC4 515-137892)	1767214390437753600	Nov. 8, 2022	1800	63	96

Table 2. Line Data and Equivalent Widths

Star	Species	Wavelength (nm)	$\log gf$	χ (eV)	W (pm)
HD 4306	Sr II	1003.665	−1.310	1.805	1.33
HD 4306	Sr II	1032.731	−0.350	1.839	6.96
HD 4306	Si I	1037.126	−0.705	4.930	3.06
HD 4306	Si I	1058.514	0.012	4.954	7.73
HD 4306	Si I	1060.343	−0.305	4.930	5.19

The whole data are available at PASJ online.

Table 3. Stellar Parameters and Fe Abundances

Object	T_{eff} (K)	$\log g$	[Fe/H]	v_{turb} (km s ⁻¹)	ref. *	[Fe/H] _{ref}	[Fe/H] _{opt}	N_{opt}	σ_{opt}	[Fe/H] _{IRD}	N_{IRD}	[Fe/H] _{fin}
HD 4306	4810	1.8	-2.9	1.6	1	-2.89	-3.02	57	0.09	-2.78	1	-3.02
HD 6268	4600	1.0	-2.6	2.1	1	-2.62	-2.71	49	0.10	-2.36	5	-2.71
HD 8724	4500	1.2	-2.0	1.8	2	-1.84				-1.92	22	-1.84
HD 13979	4830	1.6	-2.7	1.6	3	-2.97	-2.86	94	0.08	-2.73	1	-2.86
HD 85773	4370	0.7	-2.4	2.0	4,5	-2.43	-2.52	57	0.09	-2.42	11	-2.52
HD 88609	4550	1.1	-3.1	2.4	1,6	-3.06	-3.10	51	0.16	-2.94	2	-3.10
HD 107752	4800	1.6	-2.8	1.9	4,5	-2.77	-2.81	80	0.13	-2.75	2	-2.81
HD 108577	5050	1.6	-2.2	1.9	4,5	-2.23	-2.23	76	0.09	-2.13	6	-2.23
HD 110184	4240	0.3	-2.5	2.1	1	-2.51	-2.63	25	0.11	-2.55	11	-2.63
HD 115444	4720	1.5	-2.9	1.7	1	-2.84	-2.99	56	0.12	-2.94	4	-2.99
HD 118055	4400	1.0	-1.8	2.3	7	-1.80	-1.87	22	0.06	-1.85	29	-1.87
HD 122563	4570	1.1	-2.8	2.1	1,8	-2.76	-2.79	63	0.14	-2.63	5	-2.79
HD 187111	4450	1.1	-1.6	1.9	7	-1.60	-1.60	18	0.08	-1.60	31	-1.60
HD 204543	4600	1.0	-1.9	2.2	9	-1.86	-1.93	52	0.14	-1.91	17	-1.93
HD 221170	4510	1.0	-2.2	2.1	10	-2.19	-2.12	101	0.13	-2.22	13	-2.12
HD 237846	5015	2.0	-2.8	1.6	4,5	-2.81	-2.81	80	0.15	-2.76	3	-2.81
BD+03°2782	4600	1.5	-2.0	1.8	2	-2.03				-2.04	14	-2.03
BD+30°2611	4200	1.0	-1.5	1.8	4,5	-1.53	-1.48	20	0.08	-1.47	38	-1.48
BD+44°493	5430	3.4	-3.8	1.3	11	-3.80	-3.83	179	0.13			-3.83
BD+80°245	5225	3.0	-2.1	1.3	12	-2.07	-2.02	198	0.11	-2.00	6	-2.02
BD-02°5957	4360	0.5	-3.1	2.4	13	-3.13	-3.05	79	0.16	-3.09	2	-3.05
BD-07°2674	4500	0.7	-3.2	2.3	14	-3.16	-3.10	255	0.15	-2.94	5	-3.10
BD-14°5890	4890	2.0	-2.2	1.7	4,5	-2.16	-2.16	83	0.10	-2.12	6	-2.16
BD-15°5781	4550	0.7	-2.9	1.7	3	-2.87	-2.76	102	0.08	-2.72	3	-2.76
BD-18°271	4230	0.4	-2.6	2.5	4,5	-2.58	-2.64	50	0.09	-2.55	15	-2.64
BD-18°5550	4660	1.1	-3.2	1.6	3	-3.20	-3.03	107	0.09	-2.69	2	-3.03
BD-20°6008	4540	0.7	-3.1	1.7	3	-3.00	-2.86	86	0.08	-2.72	1	-2.86
CS 29502-092	5000	2.1	-2.8	1.8	15	-2.76	-2.87	171	0.17	-2.93	3	-2.87
CS 30314-067	4400	0.7	-2.9	2.5	15	-2.85	-2.97	111	0.15	-2.95	3	-2.97
CS 31082-001	4790	1.8	-2.8	1.9	1	-2.80	-2.88	48	0.09	-2.71	4	-2.88
HE 1116-0634	4400	0.1	-3.7	2.4	16	-3.73	-3.66	86	0.18	-3.68	2	-3.66
HE 1320-1339	4690	1.2	-2.9	1.8	3	-2.93	-3.04	107	0.07	-3.12	2	-3.04
HE 1523-0901	4500	0.8	-2.8	2.4	13	-2.83	-2.79	74	0.14	-2.87	3	-2.79
LAMOST J0032+4107	5070	2.2	-2.7	1.8	17	-2.69	-2.62	123	0.11	-2.74	1	-2.62
LAMOST J0040+2729	4574	1.3	-2.8	2.2	17	-2.80	-2.69	130	0.11	-2.70	2	-2.69
LAMOST J0748+4613	4700	1.3	-3.1	2.2	17	-3.10	-3.02	131	0.12	-2.99	2	-3.02
LAMOST J2109+1725	4940	2.1	-2.7	1.7	17	-2.57	-2.50	146	0.10	-2.39	1	-2.50
LAMOST J2114-0616	4727	1.7	-2.6	1.8	17	-2.55	-2.48	105	0.09	-2.25	3	-2.48
LAMOST J2217+2104	4500	0.9	-3.9	2.3	18	-3.90	-3.93	53	0.16			-3.93
LAMOST J2347+2851	4864	1.9	-2.4	1.8	17	-2.36	-2.27	139	0.10	-2.22	2	-2.27
2MASS J0643+5934	4900	2.5	-2.9	1.5	19	-2.90						-2.90
2MASS J0954+5246	4340	0.4	-3.0	2.3	20	-2.99	-2.94	104	0.11	-2.78	6	-2.94
2MASS J2016-0507	4585	0.9	-2.9	2.9	13	-2.89	-2.81	80	0.18	-2.72	5	-2.81
2MASS J2145+1249	4580	0.5	-3.3	2.7	21	-3.10				-3.09	3	-3.10

* References – 1: Honda et al. (2004); 2: Burris et al. (2000); 3: Roederer et al. (2014); 4: Ishigaki et al. (2012); 5: Ishigaki et al. (2013); 6: Honda et al. (2007); 7: Fulbright (2000); 8: Honda et al. (2006); 9: Aoki & Honda (2008); 10: Ivans et al. (2006); 11: Ito et al. (2013); 12: Ivans et al. (2003); 13: Hansen et al. (2018); 14: Cain et al. (2018); 15: Aoki et al. (2002a); 16: Hollek et al. (2011); 17: Li et al. (2022); 18: Aoki et al. (2018); 19: Bandyopadhyay et al. (2022); 20: Holmbeck et al. (2018); 21: Placco et al. (2019)

Table 4. Abundance Sensitivity to Stellar Parameters

Element	ΔT_{eff} (+100K)	$\Delta \log g$ (+0.3 dex)	Δv_{turb} (+0.3 km s ^{−1})	$\Delta [\text{Fe}/\text{H}]$ (+0.3 dex)	$\sigma_{\log \epsilon}$	$\sigma_{[\text{X}/\text{Fe}]}$
HD 221170						
Mg	+0.11	−0.08	−0.15	+0.06	0.22	0.11
Al	+0.07	−0.03	−0.02	+0.06	0.09	0.09
Si	+0.08	0.01	−0.10	+0.02	0.13	0.09
Fe	+0.14	−0.02	−0.07	+0.05	0.17	...
Sr	+0.02	−0.14	−0.24	−0.06	0.29	0.29
2MASS J0954+5246						
Na	+0.05	0.13	−0.22	−0.02	0.26	0.25
Mg	+0.09	−0.04	−0.09	+0.02	0.13	0.08
Al	+0.07	−0.03	−0.01	+0.02	0.07	0.11
Si	+0.07	0.06	−0.06	+0.01	0.10	0.09
Fe	+0.16	−0.04	−0.07	+0.01	0.18	...
Sr	+0.05	0.13	−0.22	−0.02	0.26	0.25

Table 5. Mg Abundances

Object	$\log \epsilon(\text{Mg})$	[Mg/Fe]	N	σ	Error _{total}
HD 4306	5.19	+0.61	3	0.18	0.13
HD 6268	5.49	+0.60	3	0.13	0.11
HD 8724	6.19	+0.43	2	...	0.14
HD 13979	5.20	+0.46	3	0.18	0.11
HD 85773	5.50	+0.42	5	0.17	0.13
HD 88609	5.17	+0.67	4	0.12	0.12
HD 107752	5.15	+0.36	3	0.03	0.11
HD 108577	5.79	+0.42	4	0.15	0.14
HD 110184	5.53	+0.56	5	0.09	0.12
HD 115444	5.16	+0.55	4	0.05	0.10
HD 118055	6.13	+0.40	5	0.12	0.12
HD 122563	5.30	+0.49	6	0.09	0.09
HD 187111	6.64	+0.64	2	...	0.16
HD 204543	6.17	+0.50	5	0.09	0.12
HD 221170	5.88	+0.41	6	0.06	0.11
HD 237846	5.09	+0.30	7	0.11	0.09
BD+03°2782	5.90	+0.33	8	0.18	0.13
BD+30°2611	6.38	+0.26	7	0.09	0.11
BD+44°493	4.51	+0.74	3	0.09	0.10
BD+80°245	5.39	−0.19	6	0.11	0.12
BD−02°5957	5.06	+0.51	7	0.10	0.09
BD−07°2674	5.01	+0.51	6	0.16	0.10
BD−14°5890	5.96	+0.52	5	0.16	0.13
BD−15°5781	5.07	+0.23	3	0.12	0.12
BD−18°271	5.53	+0.57	6	0.14	0.12
BD−18°5550	5.15	+0.58	3	0.13	0.11
BD−20°6008	5.38	+0.64	3	0.23	0.13
CS 29502−092	5.01	+0.28	5	0.03	0.08
CS 30314−067	4.98	+0.35	4	0.09	0.12
CS 31082−001	5.27	+0.55	5	0.12	0.10
HE 1116−0634	4.70	+0.76	3	0.15	0.10
HE 1320−1339	5.01	+0.45	4	0.06	0.11
HE 1523−0901	5.06	+0.25	6	0.16	0.10
LAMOST J0032+4107	4.99	+0.01	2	...	0.12
LAMOST J0040+2729	5.29	+0.39	4	0.15	0.09
LAMOST J0748+4613	4.92	+0.34	8	0.16	0.10
LAMOST J2109+1725	5.56	+0.46	4	0.11	0.10
LAMOST J2114−0616	5.49	+0.37	6	0.08	0.12
LAMOST J2217+2104	5.00	+1.33	7	0.12	0.09
LAMOST J2347+2851	5.69	+0.36	4	0.05	0.13
2MASS J0643+5934	5.43	+0.73	3	0.19	0.13
2MASS J0954+5246	5.22	+0.57	8	0.10	0.09
2MASS J2016−0507	5.12	+0.33	6	0.07	0.08
2MASS J2145+1249	5.10	+0.60	6	0.10	0.09

Table 6. Si Abundances

Object	$\log \epsilon(\text{Si})$	[Si/Fe]	N	σ	Error _{total}
HD 4306	5.25	+0.76	19	0.11	0.10
HD 6268	5.48	+0.68	25	0.13	0.10
HD 8724	6.16	+0.49	29	0.13	0.09
HD 13979	5.40	+0.75	21	0.14	0.10
HD 85773	5.53	+0.54	26	0.20	0.10
HD 88609	5.16	+0.74	14	0.19	0.11
HD 107752	5.14	+0.44	16	0.14	0.10
HD 108577	5.86	+0.58	27	0.19	0.10
HD 110184	5.51	+0.63	27	0.16	0.09
HD 115444	5.05	+0.53	14	0.13	0.10
HD 118055	6.06	+0.43	29	0.13	0.09
HD 122563	5.29	+0.57	24	0.11	0.10
HD 187111	6.36	+0.45	24	0.17	0.09
HD 204543	6.16	+0.58	27	0.17	0.09
HD 221170	5.82	+0.44	29	0.14	0.09
HD 237846	5.10	+0.40	16	0.14	0.10
BD+03° 2782	5.97	+0.49	27	0.17	0.09
BD+30° 2611	6.57	+0.54	25	0.19	0.10
BD+44° 493	4.18	+0.50	5	0.12	0.11
BD+80° 245	5.17	−0.32	12	0.07	0.09
BD−02° 5957	5.00	+0.54	14	0.11	0.10
BD−07° 2674	5.06	+0.65	14	0.10	0.10
BD−14° 5890	5.85	+0.50	26	0.18	0.09
BD−15° 5781	5.26	+0.51	15	0.15	0.10
BD−18° 271	5.44	+0.57	26	0.14	0.09
BD−18° 5550	5.11	+0.63	18	0.13	0.10
BD−20° 6008	5.26	+0.61	20	0.18	0.10
CS 29502−092	4.93	+0.29	11	0.08	0.10
CS 30314−067	5.04	+0.50	15	0.18	0.10
CS 31082−001	5.30	+0.67	18	0.11	0.10
HE 1116−0634	4.52	+0.66	12	0.10	0.10
HE 1320−1339	5.20	+0.73	19	0.14	0.10
HE 1523−0901	5.11	+0.39	16	0.14	0.10
LAMOST J0032+4107	5.29	+0.40	9	0.13	0.10
LAMOST J0040+2729	5.34	+0.53	24	0.10	0.10
LAMOST J0748+4613	5.00	+0.52	15	0.07	0.09
LAMOST J2109+1725	5.51	+0.50	19	0.12	0.10
LAMOST J2114−0616	5.65	+0.62	22	0.18	0.10
LAMOST J2217+2107	4.33	+0.75	12	0.12	0.10
LAMOST J2347+2851	5.71	+0.47	24	0.15	0.09
2MASS J0643+5934	5.55	+0.94	12	0.21	0.11
2MASS J0954+5246	5.18	+0.61	21	0.11	0.10
2MASS J2016−0507	5.03	+0.33	15	0.12	0.10
2MASS J2145+1249	4.95	+0.54	15	0.09	0.10

Table 7. Na Abundances

Object	$\log \epsilon(\text{Na})$	[Na/Fe]	N	Error _{total}
HD 8724	4.49	+0.09	1	0.18
HD 85773	3.89	+0.17	1	0.23
HD 108577	4.19	+0.18	1	0.22
HD 110184	3.80	+0.42	2	0.17
HD 118055	4.44	+0.08	2	0.15
HD 122563	3.59	+0.14	1	0.15
HD 187111	4.67	+0.03	1	0.21
HD 204543	4.41	+0.10	1	0.21
HD 221170	3.86	−0.26	1	0.19
BD+30 2611	4.73	−0.03	1	0.22
BD-14 5890	4.46	+0.38	1	0.22
2MASS J0954+5246	3.62	+0.32	1	0.14

Table 8. Al abundances

Object	$\log \epsilon(\text{Al})$	[Al/Fe]	N	σ	Error _{total}
HD 4306	3.30	−0.13	1	...	0.16
HD 6268	3.79	+0.05	2	...	0.14
HD 8724	4.66	+0.05	3	0.11	0.12
HD 13979	3.73	+0.14	2	...	0.15
HD 85773	4.01	+0.08	4	0.09	0.14
HD 88609	3.61	+0.26	1	...	0.22
HD 108577	3.91	−0.31	1	...	0.21
HD 110184	3.99	+0.17	3	0.14	0.13
HD 118055	4.62	+0.04	3	0.09	0.12
HD 122563	3.92	+0.26	3	0.14	0.13
HD 187111	5.26	+0.41	4	0.21	0.12
HD 204543	4.82	+0.30	4	0.20	0.12
HD 221170	4.34	+0.01	3	0.08	0.12
BD+03°2782	4.59	+0.17	5	0.18	0.12
BD+30°2611	5.07	+0.10	6	0.28	0.12
BD−02°5957	3.64	+0.24	1	...	0.16
BD−14°5890	4.22	−0.07	4	0.12	0.13
BD−18°271	4.14	+0.33	2	...	0.13
CS 31082−001	3.42	−0.15	2	...	0.14
HE 1523−0901	3.60	−0.07	1	...	0.18
LAMOST J0032+4107	0
LAMOST J0040+2729	3.78	+0.02	3	0.16	0.13
LAMOST J2109+1725	3.64	−0.31	2	...	0.14
LAMOST J2114−0616	3.76	−0.21	3	0.12	0.14
LAMOST J2347+2851	4.17	−0.01	4	0.10	0.12
2MASS J0954+5246	3.61	+0.10	3	0.19	0.13
2MASS J2016−0507	3.53	−0.11	1	...	0.16
2MASS J2145+1249	3.81	+0.46	2	...	0.13

Table 9. Sr abundances

Object	$\log \epsilon(\text{Sr})$	[Sr/Fe]	N	σ	Error _{total}
HD 4306	0.35	+0.50	3	0.09	0.26
HD 6268	1.17	+1.01	3	0.20	0.26
HD 8724	1.79	+0.76	3	0.14	0.30
HD 13979	0.59	+0.58	2	...	0.27
HD 85773	1.16	+0.81	3	0.26	0.31
HD 88609	0.70	+0.92	3	0.10	0.28
HD 107752	0.77	+0.71	2	...	0.27
HD 108577	1.41	+0.77	3	0.27	0.31
HD 110184	1.36	+1.12	3	0.19	0.30
HD 115444	0.60	+0.72	3	0.09	0.26
HD 118055	1.68	+0.68	3	0.12	0.30
HD 122563	0.72	+0.64	3	0.14	0.26
HD 187111	1.94	+0.67	3	0.17	0.30
HD 204543	1.83	+0.89	3	0.17	0.30
HD 221170	1.41	+0.66	3	0.14	0.30
HD 237846	0.40	+0.34	3	0.08	0.27
BD+03 2782	1.88	+1.04	3	0.13	0.30
BD+30 2611	2.35	+0.96	3	0.23	0.31
BD+80 245	0.12	−0.73	1	...	0.30
BD−02 5957	0.67	+0.85	3	0.14	0.26
BD−07 2674	0.36	+0.59	3	0.09	0.26
BD−14 5890	1.40	+0.69	3	0.15	0.31
BD−15 5781	0.83	+0.72	3	0.22	0.27
BD−18 271	0.98	+0.75	3	0.16	0.30
BD−18 5550	−0.51	−0.35	2	...	0.27
BD−20 6008	0.56	+0.55	3	0.24	0.27
CS 29502−092	0.07	+0.07	2	...	0.26
CS 30314−067	0.30	+0.40	3	0.06	0.27
CS 31082−001	1.32	+1.33	3	0.15	0.26
HE 1320−1339	0.94	+1.11	3	0.21	0.27
HE 1523−0901	1.20	+1.12	3	0.12	0.27
LAMOST J0032+4107	1.07	+0.82	1	...	0.28
LAMOST J0040+2729	1.10	+0.93	3	0.12	0.26
LAMOST J0748+4613	0.23	+0.38	3	0.07	0.26
LAMOST J2109+1725	0.50	+0.13	2	...	0.27
LAMOST J2114−0616	1.49	+1.10	3	0.22	0.31
LAMOST J2347+2851	1.45	+0.85	3	0.19	0.30
2MASS J0643+5934	1.37	+1.40	3	0.12	0.27
2MASS J0954+5246	1.00	+1.07	3	0.20	0.26
2MASS J2145+1249	0.32	+0.55	3	0.07	0.26

Table 10. Average and standard deviation of abundance ratios

	$-3.5 < [\text{Fe}/\text{H}] < -2.5$				$-2.5 < [\text{Fe}/\text{H}] < -1.5$			
	This work		Literature		This work		Literature	
	average	σ	average	σ	average	σ	average	σ
[Mg/Fe]	0.46	0.15	0.38	0.19	0.43	0.10	0.27	0.18
[Al/Fe]	0.09	0.17	-0.62	0.28	0.04	0.25	-0.80	0.24
[Si/Fe]	0.58	0.14	0.54	0.28	0.51	0.05	0.44	0.19
[Sr/Fe]	0.68	0.47	-0.26	0.58	0.74	0.19	-0.14	0.43

References

- Afşar, M., Sneden, C., Frebel, A., et al. 2016, *ApJ*, 819, 103. doi:10.3847/0004-637X/819/2/103
- Andrievsky, S. M., Spite, M., Korotin, S. A., et al. 2007, *A&A*, 464, 1081. doi:10.1051/0004-6361:20066232
- Andrievsky, S. M., Spite, F., Korotin, S. A., et al. 2011, *A&A*, 530, A105. doi:10.1051/0004-6361/201116591
- Aoki, W., Beers, T. C., Honda, S., et al. 2022, *PASJ*, 74, 273. doi:10.1093/pasj/psab123
- Aoki, W. & Honda, S. 2008, *PASJ*, 60, L7. doi:10.1093/pasj/60.3.L7
- Aoki, W., Matsuno, T., Honda, S., et al. 2018, *PASJ*, 70, 94. doi:10.1093/pasj/psy092
- Aoki, W., Norris, J. E., Ryan, S. G., et al. 2002a, *ApJ*, 567, 1166. doi:10.1086/338756
- Aoki, W., Norris, J. E., Ryan, S. G., et al. 2002b, *ApJL*, 576, L141. doi:10.1086/343761
- Asplund, M., Grevesse, N., Sauval, A. J., & Scott, P. 2009, *ARA&A*, 47, 481
- Bandyopadhyay, A., Sivarani, T., Beers, T. C., et al. 2022, *ApJ*, 937, 52. doi:10.3847/1538-4357/ac8b0f
- Barklem, P. S., Christlieb, N., Beers, T. C., et al. 2005, *A&A*, 439, 129. doi:10.1051/0004-6361:20052967
- Bergemann, M., Hansen, C. J., Bautista, M., et al. 2012, *A&A*, 546, A90. doi:10.1051/0004-6361/201219406
- Biemont, E. & Brault, J. W. 1986, *Phys. Scr.*, 34, 751. doi:10.1088/0031-8949/34/6B/007
- Burris, D. L., Pilachowski, C. A., Armandroff, T. E., et al. 2000, *ApJ*, 544, 302. doi:10.1086/317172
- Cain, M., Frebel, A., Gull, M., et al. 2018, *ApJ*, 864, 43. doi:10.3847/1538-4357/aad37d
- Castelli, F. & Kurucz, R. L. 2003, *Modelling of Stellar Atmospheres*, 210, A20
- Cayrel, R., Depagne, E., Spite, M., et al. 2004, *A&A*, 416, 1117. doi:10.1051/0004-6361:20034074
- François, P., Matteucci, F., Cayrel, R., et al. 2004, *A&A*, 421, 613. doi:10.1051/0004-6361:20034140
- Fukue, K., Matsunaga, N., Kondo, S., et al. 2021, *ApJ*, 913, 62. doi:10.3847/1538-4357/abf0b1
- Fulbright, J. P. 2000, *AJ*, 120, 1841. doi:10.1086/301548
- Grevesse, N., Scott, P., Asplund, M., et al. 2015, *A&A*, 573, A27. doi:10.1051/0004-6361/201424111
- Hansen, T. T., Holmbeck, E. M., Beers, T. C., et al. 2018, *ApJ*, 858, 92. doi:10.3847/1538-4357/aabacc
- Heger, A. & Woosley, S. E. 2010, *ApJ*, 724, 341. doi:10.1088/0004-637X/724/1/341
- Hirano, T., Kuzuhara, M., Kotani, T., et al. 2020, *PASJ*, 72, 93. doi:10.1093/pasj/psaa085
- Hollek, J. K., Frebel, A., Roederer, I. U., et al. 2011, *ApJ*, 742, 54. doi:10.1088/0004-637X/742/1/54
- Holmbeck, E. M., Beers, T. C., Roederer, I. U., et al. 2018, *ApJL*, 859, L24. doi:10.3847/2041-8213/aac722
- Honda, S., Aoki, W., Ishimaru, Y., et al. 2006, *ApJ*, 643, 1180. doi:10.1086/503195
- Honda, S., Aoki, W., Ishimaru, Y., et al. 2007, *ApJ*, 666, 1189. doi:10.1086/520034
- Honda, S., Aoki, W., Kajino, T., et al. 2004, *ApJ*, 607, 474. doi:10.1086/383406
- Ishigaki, M. N., Aoki, W., & Chiba, M. 2013, *ApJ*, 771, 67. doi:10.1088/0004-637X/771/1/67
- Ishigaki, M. N., Chiba, M., & Aoki, W. 2012, *ApJ*, 753, 64. doi:10.1088/0004-637X/753/1/64
- Ishigaki, M. N., Tominaga, N., Kobayashi, C., et al. 2018, *ApJ*, 857, 46. doi:10.3847/1538-4357/aab3de
- Ito, H., Aoki, W., Beers, T. C., et al. 2013, *ApJ*, 773, 33. doi:10.1088/0004-637X/773/1/33
- Ivans, I. I., Simmerer, J., Sneden, C., et al. 2006, *ApJ*, 645, 613. doi:10.1086/504069
- Ivans, I. I., Sneden, C., James, C. R., et al. 2003, *ApJ*, 592, 906. doi:10.1086/375812
- Jacobson, H. R., Keller, S., Frebel, A., et al. 2015, *ApJ*, 807, 171. doi:10.1088/0004-637X/807/2/171
- Johnson, J. A. 2002, *ApJS*, 139, 219. doi:10.1086/338117
- Käppeler, F., Gallino, R., Bisterzo, S., et al. 2011, *Reviews of Modern Physics*, 83, 157. doi:10.1103/RevModPhys.83.157
- Kelleher, D. E. & Podobedova, L. I. 2008, *Journal of Physical and Chemical Reference Data*, 37, 1285. doi:10.1063/1.2734566
- Kerber, F., Nave, G., & Sansonetti, C. J. 2008, *ApJS*, 178, 374. doi:10.1086/590111
- Kobayashi, C., Karakas, A. I., & Lugaro, M. 2020, *ApJ*, 900, 179. doi:10.3847/1538-4357/abae65
- Kobayashi, C., Umeda, H., Nomoto, K., et al. 2006, *ApJ*, 653, 1145. doi:10.1086/508914
- Kondo, S., Fukue, K., Matsunaga, N., et al. 2019, *ApJ*, 875, 129. doi:10.3847/1538-4357/ab0ec4
- Kotani, T., Tamura, M., Nishikawa, J., et al. 2018, *Proc. SPIE*, 10702, 1070211. doi:10.1117/12.2311836
- Kupka, F., Piskunov, N., Ryabchikova, T. A., et al. 1999, *A&AS*, 138, 119. doi:10.1051/aas:1999267
- Kuzuhara, M., Hirano, T., Kotani, T., et al. 2018, *Proc. SPIE*, 10702, 1070260. doi:10.1117/12.2311832
- Li, H., Aoki, W., Matsuno, T., et al. 2022, *ApJ*, 931, 147. doi:10.3847/1538-4357/ac6514
- Li, H. N., Ludwig, H.-G., Caffau, E., et al. 2013, *ApJ*, 765, 51. doi:10.1088/0004-637X/765/1/51
- Lind, K., Asplund, M., Barklem, P. S., et al. 2011, *A&A*, 528, A103. doi:10.1051/0004-6361/201016095
- Lind, K., Nordlander, T., Wehrhahn, A., et al. 2022, *A&A*, 665, A33. doi:10.1051/0004-6361/202142195
- McWilliam, A., Preston, G. W., Sneden, C., et al. 1995, *AJ*, 109, 2757. doi:10.1086/117486
- Mendoza, C., Eissner, W., LeDourneuf, M., et al. 1995, *Journal of Physics B Atomic Molecular Physics*, 28, 3485. doi:10.1088/0953-4075/28/16/006
- Nomoto, K., Kobayashi, C., & Tominaga, N. 2013, *ARA&A*, 51, 457. doi:10.1146/annurev-astro-082812-140956
- Nordlander, T. & Lind, K. 2017, *A&A*, 607, A75. doi:10.1051/0004-6361/201730427
- Norris, J. E., Ryan, S. G., & Beers, T. C. 2001, *ApJ*, 561, 1034. doi:10.1086/323429
- Pehlivan Rhodin, A., Hartman, H., Nilsson, H., et al. 2017, *A&A*, 598, A102. doi:10.1051/0004-6361/201629849
- Placco, V. M., Santucci, R. M., Beers, T. C., et al. 2019, *ApJ*, 870, 122. doi:10.3847/1538-4357/aaf3b9
- Roederer, I. U. 2009, *AJ*, 137, 272. doi:10.1088/0004-6256/137/1/272
- Roederer, I. U., Preston, G. W., Thompson, I. B., et al. 2014, *AJ*, 147, 136. doi:10.1088/0004-6256/147/6/136
- Ruffoni, M. P., Allende Prieto, C., Nave, G., et al. 2013, *ApJ*, 779, 17. doi:10.1088/0004-637X/779/1/17
- Ryan, S. G., Norris, J. E., & Beers, T. C. 1996, *ApJ*, 471, 254. doi:10.1086/177967
- Scannapieco, C., Cescutti, G., & Chiappini, C. 2022, *MNRAS*, 516, 6075. doi:10.1093/mnras/stac2581
- Tamura, M., Suto, H., Nishikawa, J., et al. 2012, *Proc. SPIE*, 8446, 84461T. doi:10.1117/12.925885
- Tominaga, N., Umeda, H., & Nomoto, K. 2007, *ApJ*, 660, 516. doi:10.1086/513063
- Travaglio, C., Gallino, R., Arnone, E., et al. 2004, *ApJ*, 601, 864. doi:10.1086/380507
- Tsuji, T. 1978, *A&A*, 62, 29
- Wanajo, S. & Ishimaru, Y. 2006, *Nucl. Phys. A*, 777, 676. doi:10.1016/j.nuclphysa.2005.10.012
- Woosley, S. E. & Weaver, T. A. 1995, *ApJS*, 101, 181. doi:10.1086/192237
- Yong, D., Norris, J. E., Bessell, M. S., et al. 2013, *ApJ*, 762, 26